Bred Vectors and Tropical Pacific Forecast Errors in the NASA Coupled General Circulation Model

SHU-CHIH YANG

Earth System Science Interdisciplinary Center, and Department of Atmospheric and Oceanic Science, University of Maryland, College Park, College Park, and Global Modeling and Assimilation Office, NASA Goddard Space Flight Center, Greenbelt, Maryland

EUGENIA KALNAY

Department of Atmospheric and Oceanic Science, University of Maryland, College Park, College Park, Maryland

MING CAI

Department of Meteorology, The Florida State University, Tallahassee, Florida

MICHELE M. RIENECKER

Global Modeling and Assimilation Office, NASA Goddard Space Flight Center, Greenbelt, Maryland

(Manuscript received 21 December 2006, in final form 6 August 2007)

ABSTRACT

The breeding method has been implemented in the NASA Global Modeling and Assimilation Office coupled general circulation model (CGCM) in its operational configuration in which ocean data assimilation is used to initialize the coupled forecasts. Bred vectors (BVs), designed to capture the dominant growing errors in the atmosphere–ocean coupled system, are applied as initial ensemble perturbations. The potential improvement for ensemble prediction is investigated by comparing BVs with the oceanic growing errors, estimated by the one-month forecast error from the nonperturbed forecast. Results show that one-month forecast errors and BVs from the NASA CGCM share very similar features: BVs are clearly related to forecast errors in both SST and equatorial subsurface temperature—in particular, when the BV growth rate is large. Both the forecast errors and the BVs in the subsurface are dominated by large-scale structures near the thermocline. Results suggest that the forecast errors are dominated by dynamically evolving structures related to the variations of the background anomalous state, and that their shapes can be captured by BVs, especially during the strong 1997/98 El Niño. Hindcast experiments starting from January 1997 with one pair of BVs achieve a significant improvement relative to the control (unperturbed) hindcast by capturing many important features of this event, including the westerly wind burst in early 1997.

1. Introduction

During the last decade, the ability to simulate and predict El Niño–Southern Oscillation (ENSO) phenomena has greatly increased because of 1) the establishment of new types of observing systems contributing to a better understanding of the dominant physical processes and improved initial conditions, and 2) the improvement of coupled ocean–atmosphere modeling (Hayes et al. 1991; Wallace et al. 1998; McPhaden et al. 1998; Saha et al. 2006). However, there are still limitations in advancing ENSO forecast skill to several seasons ahead (Latif et al. 1993; Chang et al. 1996; Fedorov et al. 2003; Chen et al. 2004; and the special issue of the *Journal of Geophysical Research,* 1998, Vol. 103, No. C7, devoted to El Niño). These limitations arise from 1) errors in the initial conditions, 2) systematic errors/biases in the ocean–atmosphere coupled models, 3) problems with the initialization process, for example, model shocks in the initial coupling, and 4) the physical

Corresponding author address: Dr. Shu-Chih Yang, Earth System Science Interdisciplinary Center, Department of Atmospheric and Oceanic Science, University of Maryland, College Park, College Park, MD 20742.
E-mail: scyang@atmos.umd.edu

DOI: 10.1175/2007MWR2118.1

© 2008 American Meteorological Society

processes in coupled ocean–atmosphere models used to represent ENSO, including feedbacks from variabilities of different time scales (e.g., Madden–Julian oscillation; Slingo et al. 1999).

Ensemble forecasting and initialization using ocean data assimilation are, at the present, the most straightforward solutions for improving ENSO prediction (Stockdale et al. 1998; Kirtman 2003; Ji and Leetma 1997; Rosati et al. 1997; Saha et al. 2006). Ensemble forecasting systems are designed to use a set of initial perturbations to represent the uncertainties and sensitivities of the state. The ensemble mean from a well-designed ensemble forecast system is expected to improve the control forecast (without perturbations) assuming the true state can be encompassed within a set of ensemble evolutions (Toth and Kalnay 1997). In addition, the ensemble spread can be used to assess the forecasting skill (Moore and Kleeman 1998). However, at this stage, the ensemble forecasts implemented for seasonal to interannual prediction at operational centers still face the difficulty that the ensemble perturbations from a single coupled ocean–atmosphere model have limited growth at early forecast leads relative to the amplitude of mean error (Vialard et al. 2003a; Palmer et al. 2004; Saha et al. 2006). This indicates that 1) current techniques to initialize ensemble members may not be optimal and not sensitive enough to low-frequency variations, such as the seasonal-to-interannual variability and 2) the operational coupled model systems may have some serious deficiencies. However, studies of the performance of the coupled GCM suggested that the influence of the model error is relatively small in the tropical Pacific over the first month's forecast because of the better quality of the ocean analyses and higher potential predictability in this region. Saha et al. (2006) showed that the climate drift from the National Centers for Environmental Prediction (NCEP) coupled GCM in the first month forecast is small in the tropical Pacific, and Peng et al. (2004) pointed out that the relatively small drift of the first month forecast does not have a strong impact on the SST variability in equatorial Pacific. Therefore, the relatively large error of the one-month forecasts seems to suggest that the initial conditions play a critical role in the skill of the prediction.

Experiments from Moore and Kleeman (1996) showed a connection between ensemble spread and forecast skill when the ensemble perturbations are designed to increase the low-frequency ENSO variability. However, low ensemble spread would occur if random perturbations are used for the initial ensemble. Toth and Kalnay (1996) also point out that initial coupled ensemble perturbations need to be generated in such a way that they carry the slowly growing coupled instabilities for ENSO prediction. These studies illustrate the concept that the initial ensemble perturbations and their evolution should project on the dominant modes of variability of the coupled system.

Since the upper-ocean circulation is mostly a wind-driven process, the changes in sea surface temperature (SST) anomalies result from coupled atmosphere–ocean processes. Most of the current methods for generating ensemble perturbations for coupled models intend to perturb the wind to assess the uncertainties in SST fields. For example, in a tier 2 system, the atmospheric ensemble is generated under the influence of only a single SST field (Bengtsson et al. 1993). Tier 1 systems generate the ensemble members via a coupled ocean–atmospheric model in order to have the perturbation grow under a coupled configuration (e.g., Stockdale et al. 1998; Saha et al. 2006). This single-stage configuration is now widely used for operational ENSO prediction. However, there is no sophisticated way so far to use a full-physics coupled GCM to generate the initial ensemble perturbations, which are naturally "coupled" and can be projected on the growing mode related to slowly varying coupled instability. The optimal perturbations (Kleeman et al. 2003), which are computationally expensive, need to separate out fast physical processes explicitly in order to have the ENSO-related growing mode. In most of the operational centers, the ensemble perturbations used for the CGCM are mostly perturbing the atmospheric components with a set of initial atmospheric state days apart. As a result, ensemble perturbations are not optimally coupled at the initial time and a spinup time is needed to couple the oceanic and atmospheric perturbations. Such a lack of coupling in the initial ensemble perturbations would limit the initial growth of the ensemble members and their ability to depict the uncertainties in the forecasted state.

The coupled breeding technique proposed by Toth and Kalnay (1996) provides a method to derive the slowly varying, coupled instability for initial ensemble perturbations. By repeatedly rescaling and evolving the coupled bred perturbations upon the background flow with the full nonlinear coupled model, the breeding cycle is aimed at filtering out fast unwanted instabilities (like fast weather noise) and retaining the growing mode we are interested in (slowly varying coupled instabilities). A bred vector (BV) is defined as the difference between two nonlinear runs (one with bred perturbations and the other without any perturbations). By taking advantage of the fact that instabilities from a complex coupled system are characterized by different

time scales, and that their amplitudes saturate at different levels, nonlinear integrations allow the unwanted fast-growing instabilities to saturate early, and leave the slow perturbations dominating the bred perturbations.

The key to selecting the instability of interest is to use physically meaningful breeding parameters, that is, the rescaling amplitude and rescaling time interval (Toth and Kalnay 1993, 1997; Peña and Kalnay 2004). Peña and Kalnay (2004) derived bred vectors, singular vectors (SVs), and Lyapunov vectors (LVs) with experiments using fast and slow coupled Lorenz three-variable models. Their idealized coupled system was designed to mimic a coupled system including a tropical ocean, and tropical and extratropical atmospheres. They demonstrated that breeding can be used to isolate the slow modes when choosing a slow variable to measure the growth of the perturbation and when using a long interval for the rescaling, allowing the fast extratropical weather noise to saturate. In contrast, SVs and LVs are swamped by the fast-growing instabilities, since by being linear they are designed to capture the fastest-growing instability of the system. For applications to atmosphere–ocean coupled models, most studies use intermediate or hybrid coupled models to derive the SVs (optimal perturbations) for ENSO prediction. However, results from different studies are not consistent even when using the same optimization norm (i.e., SST norm with 3–6-month optimization period; Xue et al. 1994; Chen et al. 1997; Fan et al. 2000; Moore and Kleeman 1997a,b). Besides the concern of constructing the tangent linear–adjoint of the complex matrix operator of the CGCM, there is a major difficulty in separating the ENSO-related SVs from the unwanted growing modes. This problem is not encountered when dealing with the simplified physics used in intermediate models. When applying this method to CGCMs, particular care needs to be taken to filter out the fast-growing modes of weather instability in order to obtain the "climate relevant SVs." Kleeman et al. (2003) and Tang et al. (2006) derived such SVs with an ensemble of 20–30 members in a reduced space based on the first five EOF modes of Pacific SST anomalies.

The coupled breeding experiments of Cai et al. (2003) with a Cane–Zebiak intermediate coupled model, and of Yang et al. (2006) with the coupled general circulation model (CGCM) developed at the National Aeronautics and Space Administration (NASA) Goddard Space Flight Center gave very similar robust conclusions. In these breeding experiments, all the dynamical variables in both atmospheric and oceanic components are perturbed so that coupled nonlinear processes are naturally included. Both studies show that ENSO bred vectors and their growth rate are sensitive to the background ENSO evolution, and that the dominant fast-growing mode in the SST appears in the eastern equatorial Pacific. Moreover, Yang et al. (2006) confirmed that the characteristics of bred vectors from two independently developed CGCMs [NASA and National Oceanic and Atmospheric Administration (NOAA)/NCEP] have a similar structure, not only in the tropical Pacific basin but also in the atmospheric ENSO-teleconnected region. These findings suggest that the perturbations derived from breeding runs are representative of the coupled atmospheric and oceanic changes associated with the ENSO variability. Cai et al. (2003) also showed that using a pair of positive/negative BVs as the ensemble perturbations, the "spring barrier"[1] in ENSO forecast skill could be substantially reduced.

Although the results of these studies were encouraging, the coupled breeding experiments were performed under a perfect model scenario. In this paper we extend the coupled breeding technique to a realistic scenario: performing breeding cycles in the NASA operational CGCM with real, noisy observations assimilated into the ocean component. We then explore the potential applications for ensemble forecasting and ocean data assimilation initialization of the CGCM, by reducing or alleviating the growing errors that appear to be in the initial conditions. We hypothesize that the uncertainties related to coupled instabilities appear in the coupled forecasts after integrating the CGCM beyond the time scale of weather synoptic instabilities. Therefore, the first goal in this study is to test whether BVs (representing the leading coupled instabilities) can be used to represent the structure of the short-range (about one month) coupled forecast error. If BVs turn out to be similar to forecast errors then they have potential for use in ensemble forecasting and in reducing the coupled forecast errors at a longer forecast lead time, for example, the 12-month forecast. Another goal in our study is to explore the potential to incorporate bred vectors with operational ocean data assimilation for better use of the observations to provide better oceanic analyses (initial conditions) for coupled forecasting. The current ocean data assimilation in the NASA operational system uses an optimal interpolation (OI) scheme. The background error covariance used in the OI scheme is a statistical estimation of the forecast error structure averaged in time and therefore it is flow independent. A data assimilation scheme with a time-

[1] "Spring barrier" is a common feature of a sudden drop of forecast skill for the forecasts that begin in the spring and pass through the summer.

independent background error covariance may underestimate sudden changes of the background flow due to the dynamical instabilities. Advanced oceanic data assimilation schemes carrying flow-dependent error statistics, like ensemble ocean data assimilation (Evensen 2003; Keppenne and Rienecker 2002, 2003; Keppenne et al. 2005) or four-dimensional variational data assimilation (4DVAR; Weaver et al. 2003; Vialard et al. 2003b), have shown their advantages in the tropical Pacific and have a positive impact on the ENSO forecasts. However, even in these advanced methods, it is difficult to include the impact from *coupled* processes needed for better initialization for ENSO prediction when constructing the background error covariance. In either the ensemble Kalman filter or 4DVAR, the observed wind is used as the forcing field, that is, a fixed atmospheric condition. Therefore, the uncertainties due to the coupled processes are not included in the background error covariance (e.g., the uncertainties in the wind forcing do not include the feedbacks from the ocean state). Also, the computational cost of these advanced techniques is still a major concern.

Such dynamically coupled errors can be incorporated within the data assimilation scheme with the bred ensemble (described in full model space) by augmenting their structures with the original uncoupled background error covariance. Such a hybrid-type assimilation is easier to implement on the (multivariate/univariate) OI and ensemble Kalman filter. In principle, it would also be possible to include them in the cost function defined in a 4DVAR system, thus allowing the background error covariance to have state-dependent structures (Lorenc 2003; Buehner 2005; Wang et al. 2007). Therefore, we propose to test the use of bred vectors obtained from the CGCM to provide information related to coupled error structures at a very low computational cost. If indeed there are similarities between bred vectors and forecast errors (which we will determine according to our first goal), BVs have the potential to provide information related to the slowly varying, coupled error structure in the OI scheme by augmenting the time-independent background structure with flow-dependent structure (Corazza et al. 2003; Yang et al. 2007).

Our paper is organized as follows. In section 2, we briefly introduce the NASA coupled GCM used for experimental forecasts and the setup of the coupled breeding experiments. Section 3 describes the relationship between bred vectors and forecast errors. The application of bred vectors in ocean data assimilation scheme is discussed in section 4. The summary and discussion are given in section 5.

2. Description of the breeding experiments in the GMAO operational system

a. The NASA GMAO coupled GCM

The Global Modeling and Assimilation Office (GMAO) coupled model is a fully coupled global ocean–atmosphere–land system developed at the NASA Goddard Space Flight Center (GSFC; Vintzileos et al. 2003). It comprises the NASA Seasonal-to-Interannual Prediction Project atmospheric general circulation model (NSIPP AGCM; Takacs and Suarez 1996; Bacmeister and Suarez 2002; Bacmeister et al. 2000), the Poseidon ocean model (OGCM; Schopf and Loughe 1995; Yang et al. 1999), and the Mosaic land surface model (LSM; Koster and Suarez 1992), all developed for the purpose of improving seasonal to interannual prediction.

The model variables of the ocean GCM are arranged on isopycnal layers; they are thickness, temperature, zonal and meridional current velocity, and salinity. The oceanic grid resolution is $5/8°$ in longitude, $1/3°$ in latitude, and 27 layers in vertical. The model variables of the atmospheric components are prescribed in sigma coordinates; they are surface pressure, zonal and meridional wind, potential temperature, and specific humidity. The atmospheric grid resolution is 2.5° in longitude, 2.0° in latitude, and 34 levels in vertical. Detailed descriptions of the coupled model and the model performances for climate variabilities can be found online at http://gmao.gsfc.nasa.gov/cgi-bin/products/climateforecasts/index.cgi.

In this study, breeding experiments are performed in the operational configuration, where the ocean is initialized with a univariate OI analysis scheme, assimilating daily subsurface temperature observations from the global XBT data (Troccoli et al. 2003). To maintain the relationship between temperature and salinity to conserve water mass properties, the local salinity profile from the model is then adjusted by the temperature analysis increment according to the method of Troccoli and Haines (1999). During the assimilation process, the SST is strongly relaxed to the SST of Reynolds et al. (2002), referred to hereafter as "Reynolds SST."

For the coupled forecasts, the atmospheric and land states are initialized independently from the ocean, and from the Atmospheric Model Intercomparison Project (AMIP) runs (Gates 1992), whose fields are obtained with the Reynolds SST specified as the boundary condition and interpolated into the AGCM resolution. Prior to coupling, the atmospheric state spins up for one day from the AMIP initial fields. The ocean is then initialized by this daily averaged wind stress, which al-

lows the ocean to include the memory of past wind, and is important for maintaining the subsurface structure and reducing climate drift and initial shock (Latif et al. 1993; Schneider et al. 1999).[2] From the results of coupled forecasts, one of the benefits of updating the ocean initial condition with the OI scheme is a reduction of the cold seasonal drift in the early forecast months, in particular for the tropical central to western Pacific.

In the operational forecasting system, the GMAO coupled GCM is used for forecasts of 12-month duration with six ensemble members. The six ensemble members include three oceanic perturbed, two atmospheric perturbed and one unperturbed initial conditions. The oceanic perturbations are generated as the difference between two randomly chosen analysis states for the ocean initial condition (within a 5-day window) and the atmospheric perturbations are randomly chosen AMIP states (restart files). The results from the hindcast experiments show that the prediction skill has a strong dependence on the seasonal cycle. For example, the prediction of the Niño-3 SST anomaly index has the best prediction skill (in terms of anomaly correlation and mean error) when starting from the cold phase of the annual cycle in the tropical eastern Pacific, especially when starting from September. On the other hand, a large mean forecast SST error is observed at early forecast leads when the coupled GCM starts from May–June, a time in which SST is rapidly cooling and before the strong cold equatorial tongue is established. In addition, except for the cases starting from September, the operational ensemble exhibits rather small spread at early forecast leads and is insensitive to season. The forecast of heat content exhibits skill similar to that of SST in the tropical eastern Pacific. The forecast heat content in the western Pacific shows good skill in the early forecast months starting from February to June. However, the ensemble spread is still very limited in the subsurface equatorial region and is far from the level of the mean anomaly forecast error. In addition, and in contrast to the real evolution, the forecast state in the eastern Pacific does not seem to benefit from the memory of the western Pacific evolution, with SST anomalies dominated by local processes for February–June starting months, and minimal coupling between the surface and the thermocline (Galanti et al. 2002). These observations provide some clues that the imperfect model physics are unable to represent the mixed layer very well when the thermocline is very shallow. They also indicate the need for ensemble perturbations that reflect seasonal uncertainties.

Based on these considerations, the main comparisons between bred vectors and forecast errors will first focus on their evolution within the oceanic component, including the surface and subsurface variations. The oceanic growing error is defined as the difference between the instantaneous fields after a one-month forecast and the corresponding analysis. The control forecast is initialized from the unperturbed initial condition.

b. *Breeding experiment*

As discussed in section 1, initial perturbations generated through coupled breeding are designed to include the growing errors associated with the slowly varying, coupled instabilities in order to capture uncertainties when predicting seasonal to interannual variations. In the breeding cycle, there are two parameters allowing us to select the growing instability of interest: 1) the rescaling period and 2) the size of rescaling norm (Toth and Kalnay 1996; Peña and Kalnay 2004; Yang et al. 2006; Vikhliaev et al. 2007). The choice of these parameters needs to be based on physical considerations (see the discussion related to Fig. 1 in Yang et al. 2006). For our purpose, a rescaling period of at least two weeks is required to allow the fast-growing weather signals to saturate and, at the same time, keep the slow, coupled instability in the bred perturbations. Vikhliaev et al. (2007) obtained similar results rescaling the bred perturbations from the COLA coupled GCM every six months with a norm measuring the growth of upper-ocean heat content.

The procedure we used to perform the breeding cycle in the GMAO operational system is the same as described in Yang et al. (2006), with a rescaling period of one month. The period used for experimental breeding and control (nonperturbed) forecasts is January 1993 to November 1998. The choice of a one-month rescaling period is fairly reasonable according to the error statistics from this coupled GCM. SST errors from operational ensemble forecasts have their fastest growth on the first month and grow much more slowly after two months. Climate drift has little impact on the relative error growth rate in the early forecast and removing it mainly reduces the magnitude of the mean error. At the beginning of the breeding cycle, the initial oceanic perturbations are obtained from the difference between two randomly chosen oceanic analysis states and the atmospheric perturbations from the differences between two randomly chosen AMIP restarts (the initial conditions of the AGCM). This set of initial perturba-

[2] Despite the one-day coupling, the introduction of a different atmosphere produces a short-lived "coupling shock." In this work we assume that since the BVs are rescaled with a period long enough to recover from the coupling shock, they are not fundamentally affected by it.

tion is rescaled to have the same amplitude of the rescaling norm.

During the coupled breeding cycle, all the model variables in the ocean and atmospheric components are perturbed. The oceanic-bred perturbations are added to oceanic analysis fields, and atmospheric bred perturbations are added to the AMIP atmospheric restart fields. After one month of coupled integration, the coupled bred perturbation is computed as the difference between the one-month perturbed and unperturbed (control) forecasts, and is rescaled to its initial amplitude according the chosen rescaling norm. The rescaled perturbation is then added to the next oceanic and atmospheric initial conditions. In our standard breeding cycle, the rescaling factor is the inverse of the growth of the RMS SST perturbation in the Niño-3 region (5°S–5°N, 150°–90°W) after one month and is applied globally to all oceanic and atmospheric variables. The process is repeated throughout the breeding period (January 1993 to November 1998). Bred vectors are the difference between the one-month perturbed and unperturbed (control) forecasts and they provide an estimate of the structure of growing instabilities, which presumably are also generating forecast errors. It is important to keep in mind that bred vectors are generated without any information about the observations used to estimate the new analysis state.

The breeding rescaling amplitude–period is chosen to separate the instabilities and avoid the nonlinear saturation and does not affect the bred structures as long as the norm is chosen according to the characteristic of the instability, and the period has to be relevant to the characteristics of the instabilities. We have performed breeding experiments with three types of rescaling norms with the amplitude chosen to be about 10% of the climate variability (i.e., the background anomaly variance), which is large enough to saturate the weather noise but detect the growth relevant to the ENSO-dominated instability. The first two experiments use global perturbations for both ocean and atmosphere states and their rescaling factors are measured by 1) the SST bred perturbations in the Niño-3 region with an amplitude of 0.1°C (the standard run), 2) the perturbation of depth of the 20°C isotherm (Z20) in the tropical Pacific with an amplitude of 0.2 m, and 3) the rescaling parameters are the same as 1) but the oceanic and atmospheric perturbations are added only in the tropical regions. Since the BV structures obtained from different rescaling norms are dominated by similar (but not identical) growing instabilities (appendix B and Yang 2005), comparisons between the structures of forecast error and bred vectors are focused on the run rescaled with the Niño-3 SST perturbations norm in the next section.

3. Observed relationship between one-month forecast error, bred vectors, and background anomaly

In this section, we illustrate the characteristics of forecast error and bred vector from this coupled system and how they evolve with the slowly varying background state (i.e., the background ENSO events). The one-month forecast error is approximated by the difference between the one-month control forecast and the analysis state verifying at the same time. This quantity represents the optimized correction to the forecast state after combining it with observational information and as such is a proxy for *forecast error.* The bred vector is derived as the difference between the perturbed forecast and the nonperturbed forecast. We will first assess whether ENSO dynamical processes dominate the evolution of both one-month forecast errors and bred vectors.

In ENSO variability, the slow dynamical processes in the ocean component play an important role in characterizing an ENSO event and, therefore, such processes should also determine the characteristics of the growing errors. This can be verified by examining the structures of forecast error and bred vector as they evolve with the background ENSO events. Several studies have indicated that the origin of an ENSO event can be traced back to *perturbations in the subsurface* of the western Pacific, which are excited by variations of the trade wind. During an El Niño event, the downwelling perturbation travels to the eastern Pacific through equatorial wave propagation, deepening the thermocline, allowing the anomalous warm water to establish, and reducing the zonal temperature gradient. The subsequent positive feedbacks from air–sea interaction then contribute to the growth of a warm episode (McPhaden et al. 1998; McPhaden 1999; Wallace et al. 1998; Boulanger and Menkes 1995). Thus, dynamical *coupled* errors in the surface layer of the eastern Pacific will not only be affected by the local processes (e.g., upwelling) but also be closely related to the errors in the subsurface state of the western Pacific, where it is also connected to the atmospheric conditions.

a. The structure of bred vector and forecast error during 1997/98 El Niño evolution

The 1997/98 El Niño is a strong warm event whose background anomaly state is characterized by distinct features of equatorial wave propagation (McPhaden

1999; McPhaden and Yu 1999). The event was triggered by a strong westerly wind burst in the western Pacific; the extreme intensity of this event has been attributed to the nonlinear interaction between ocean and atmosphere (Zhang and McPhaden 2006; Vecchi et al. 2006).

For the following analysis we select four months representing the different stages of the 1997 El Niño event (prior, developing, mature, and post stages) in order to illustrate how the forecast errors and bred vectors evolve during ENSO development. Figure 1 shows the Niño-3 index for the period October 1996 to October 1998 covering this major El Niño event that peaked at the end of 1997. Figures 1a–d are snapshots of vertical cross sections along the equator of forecast error (color shading) and bred vectors (contour) of temperature corresponding to prior, developing, mature, and post El Niño stages. As shown in Fig. 1a (the prior stage), before the warming commences the forecast error was mainly located in the subsurface of the central to western Pacific with some error also near the surface near the eastern boundary. During the developing stage, the forecast error expanded eastward and extended vertically as the warm anomaly started to build up in the eastern Pacific (Fig. 1b). At the mature stage of the event, the forecast errors were smallest near the surface near the eastern boundary and large near the thermocline (Fig. 1c). When the warm anomaly diminished and the background state returned to normal conditions, the forecast error accumulated mostly in the eastern Pacific (Fig. 1d) above the thermocline. Very similar longitude-vertical variations appear as well in the bred vectors shown with contour lines in the same figures. The bred vector evolution is characterized by an eastward propagation well synchronized with the forecast error movement, and BV shapes tend to capture the large-scale forecast error, as indicated by the collocation of forecast error and bred vector. Both the forecast error and bred vector maxima are located near the thermocline, where sharp temperature gradients can easily introduce instabilities. Such results confirm one of the important properties of BVs: local representation of the growing modes. These results also support the hypothesis that the bred vectors obtained from such a complicated CGCM with data assimilation are able to carry the information related to realistic ENSO development and that they indicate where the forecast errors will be located. We also note that since the model errors play a stronger role in the growth of the forecast errors during late spring to summer (e.g., May/01/1997 in Fig. 1d), the forecast error and BVs are less similar. Nevertheless, even without access to the observations used in estimating the analysis state and the forecast errors, the results show that the bred vector contains the dynamical instabilities that lead to the forecast errors corrected in the data assimilation.

The structure of the bred vector suggests its potential impact when used as an initial ensemble perturbation for ensemble forecasting since it projects strongly on background instabilities leading to forecast error growth. Furthermore, this suggests their potential application incorporating information on the "errors of the month" into the data assimilation process. More details and statistical diagnostics are provided in section 4.

b. The temporal and spatial relationships between bred vector, forecast error, and background variability

An important conclusion from Yang et al. (2006) and Cai et al. (2003) was that there is a relationship between the ENSO phase and the bred vector growth rate, with the maximum BV growth occurring between the two extreme phases of ENSO episodes. BV growth rate is measured as the amplitude of the BV SST in the Niño-3 region at the rescaling time (i.e., one month after coupled integration) relative to the initial amplitude and it has a nondimensional unit per month. This relationship remains valid for the BV growth rate obtained from the operational system with data assimilation. Figure 2a is the background Niño-3 index computed using the SST to indicate the temporal evolution of the ENSO episodes from 1994 to 1998. Figure 2b shows that the BV growth rates are large before and after an ENSO event, especially after the 1997 strong El Niño event, and smallest at the mature state of an ENSO event. Figure 2c is the amplitude of the forecast error in the Niño-3 region, obtained from the unperturbed initial condition, where the analysis (initial) errors are included but impossible to accurately estimate. Although the amplitudes in Figs. 2b and 2c are not directly comparable, the BV and the forecast error are dominated by similar dynamical processes; and it is seen that the temporal evolution of the BV growth rate and the forecast error have much in common, suggesting that the BV is state dependent (or sensitive to the anomalous state). As already apparent in Fig. 1, the amplitude of the forecast error is also very sensitive to the phase of ENSO and is related to background variability. During the decaying phase of the event, with rapid cooling, the BV growth rate shows a sharp increase and so does the forecast error. The change of the BV growth rate occurring before the mature phase of the 1997/98 El Niño is not as rapid as afterward but relatively large growth rate occurs during the late summer to winter of 1996 and may be related to the strong MJO activities during the same period, which contribute to trigger this strong

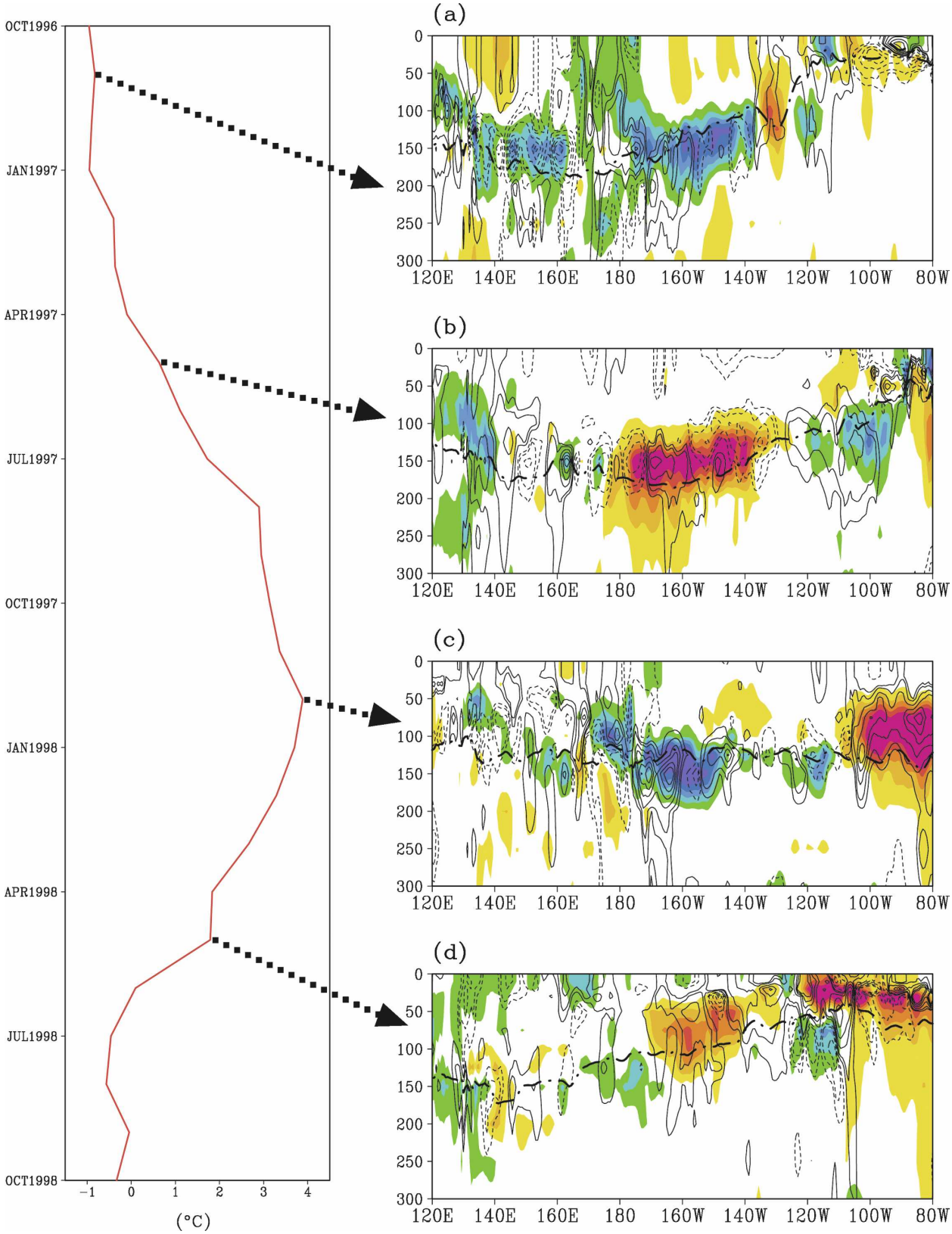
OCT1996
JAN1997
APR1997
JUL1997
OCT1997
JAN1998
APR1998
JUL1998
OCT1998
−1
0
1
2
3
4
(°C)
(a)
(b)
(c)
(d)
0
50
100
150
200
250
300
120E
140E
160E
180
160W
140W
120W
100W
80W

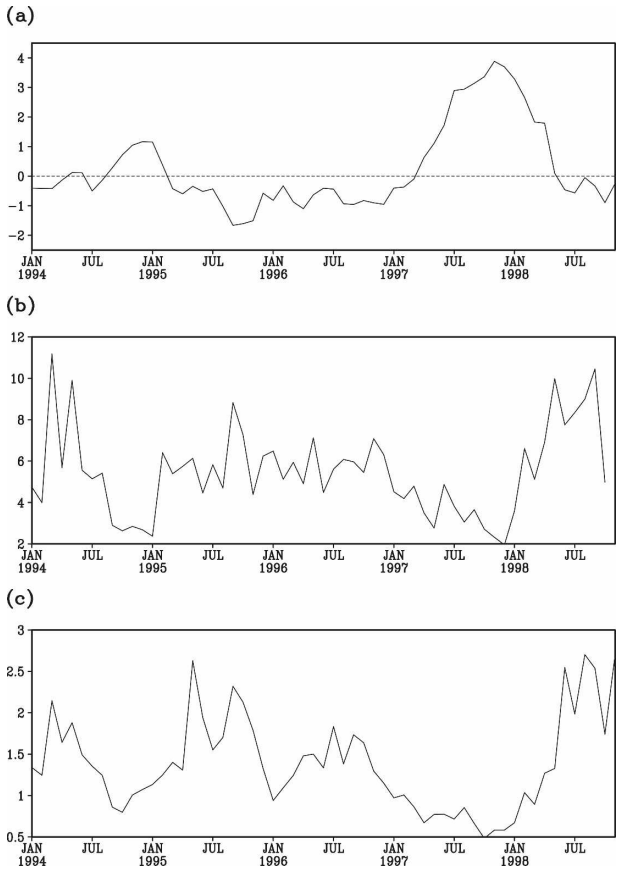

FIG. 2. (a) Background Niño-3 index (°C), (b) bred vector growth rate (month^{-1}), and (c) rms of the difference between SST analysis and one-month forecast SST in the Niño-3 region (°C).

event (Bergman et al. 2001). The relationship between these two time series suggests that the bred vector has similar behavior to the forecast error field and that bred vector growth rates can provide information related to large forecast errors, particularly when the background SST is neutral and after an ENSO event. After the anomalous ENSO warming is established in the background, error growth is inhibited because the background has reached a fairly stable state. It has been confirmed that the forecasts made by the same CGCM starting from August 1997 are very successful in capturing the subsequent temporal and spatial SST variations up to 9 months in terms of both timing and intensity (not shown).

To quantify the relationship between BV, forecast error, and background state, we used the pattern correlation between the bred vector and the forecast error in the Niño-3 region to determine to what extent the breeding method could capture such dynamical error throughout the 6 yr. The monthly pattern correlations are grouped into bins classified by BV growth rate (<2.5, 2.5–3.5, 3.5–4.5 . . . and >8.5 per month). We then calculate the mean of the absolute value of pattern correlation in each group. For comparison, the corresponding mean absolute value of the Niño-3 SST anomaly is also calculated. The absolute value is used to emphasize the phase of the ENSO event, that is, the anomalous state of the background. Figure 3 shows that the absolute value of the Niño-3 index is high when the BV growth rate is small, and close to zero when the growth rate is large, as discussed above, confirming the results of Cai et al. (2003) obtained with the ZC model. The mean pattern correlation between BVs and forecast error in the last two groups with large growth rates are significantly higher than the mean correlations of lower growth rates (with a 95% confidence level). Also, the mean background SST anomaly (absolute values) corresponding to the small growth rates (the first two groups) are higher than the values of other groups with an 80% confidence level. This suggests that when the background is in a near-neutral state, BV tend to have larger projection on the forecast error. The relatively small spatial correlation (~0.4) is due to the fact that such a complex system includes not only ENSO instabilities but also instabilities associated with shorter space and time scales and with the introduction of AMIP atmospheric initial conditions, noisy processes that could not be captured with breeding and may also be partially due to the model errors. Nevertheless, by visually comparing the structure of BV and forecast error on months with large BV growth rate, we observe that BV tends to stretch into the directions that are dominant in the forecast errors although the local maximum–minimum may not be perfectly overlapping due to the presence of multiple dynamical processes.

Combining the results from Figs. 2 and 3, we can conclude that bred vectors are naturally influenced by the background instabilities, particularly the dominant large-scale, low-frequency variabilities. The shapes of

←

FIG. 1. (left) Background Niño-3 SST index (°C) and (right) vertical cross section of the temperature forecast error (°C; color shades) and BV temperature (°C; contours) at constant depth with the depth of the 20°C isotherm denoted as the thick dash–dotted line, corresponding to (a) 1 Nov 1996, prior to ENSO stage, before warming developed; (b) 1 May 1997, the developing stage, when warming started; (c) 1 Dec 1997, the mature stage, when warming is strongest; and (d) 1 May 1998, post-ENSO stage, when the warm anomaly diminished. The contour interval is 0.5°C, and the zero contour is not plotted. The scale of the color shading is from −5° to 5°C. The amplitude within the range of −1° and 1° is not colored.

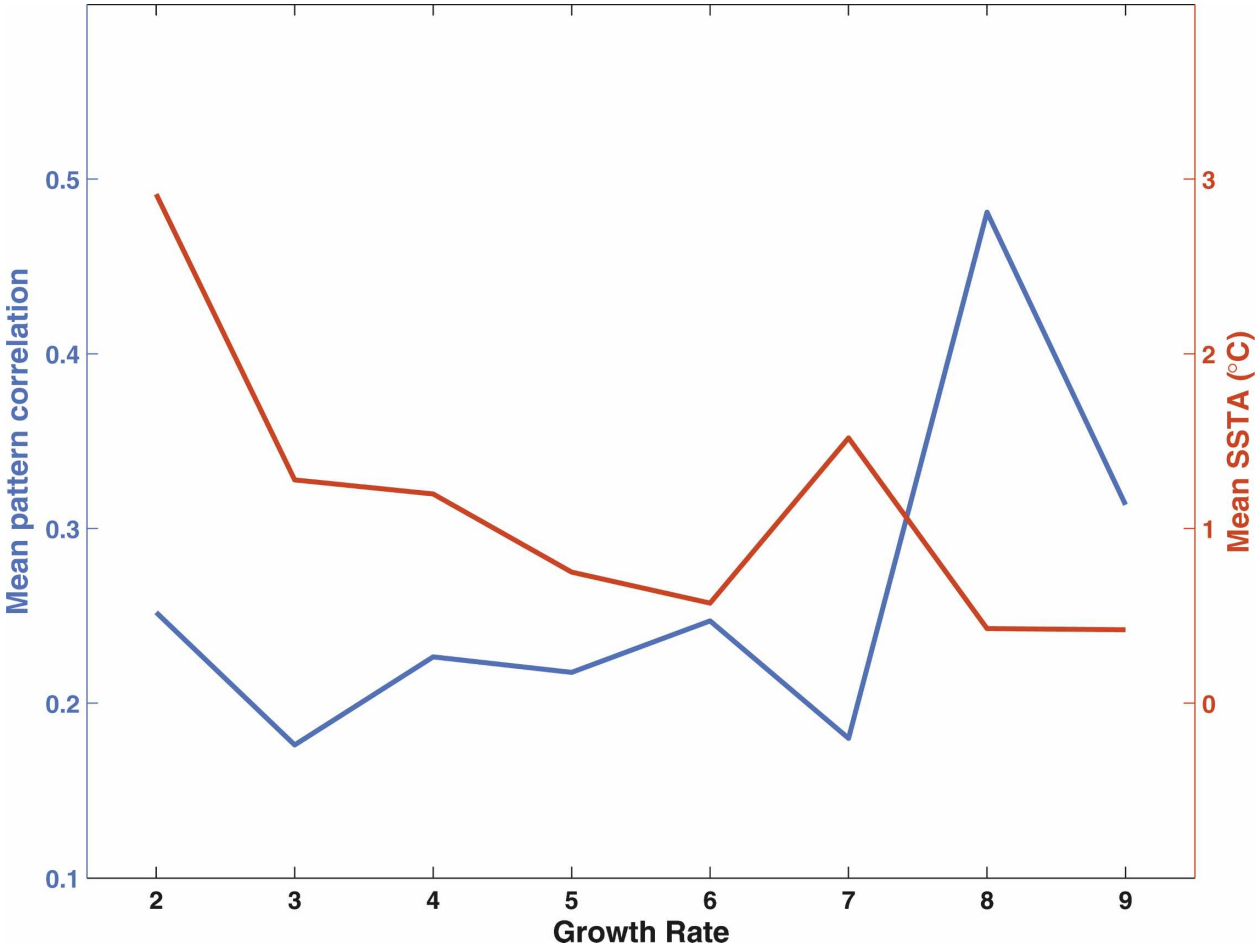

FIG. 3. Mean value of the pattern correlation (blue line) and the Niño-3 index (°C; red line) in bins defined by the BV growth rate. The pattern correlation and the Niño-3 index are grouped based on their corresponding growth rate located within the ranges of <2.5, 2.5–3.5, 3.5–4.5, . . . and >8.5. Pattern correlation is defined as the spatial correlation between the bred vector and the one-month forecast error in the Niño-3 region, and the absolute value is used for both the pattern correlation and the Niño-3 index.

forecast errors are also affected by these same instabilities. Therefore, the bred vector can detect the rapidly changing stage of the background occurring in the eastern Pacific and represent the shape of the corresponding forecast errors.

The spatial correlation between bred vectors and forecast error suggests bred vectors can be used to identify the shapes of the fast-growing instabilities that dominate the forecast error. We have examined the agreement between the bred vectors and forecast error by fitting the zonal and meridional error covariance structures with a Gaussian function (see appendix A). The correlation length derived from forecast error and bred vector illustrates the characteristic length of the "error of the month" associated with the coupled instability. Table 1 summarizes the mean value of the correlation lengths estimated from one-month forecast error and bred vector near the equator for all months. It is seen that the ranges of the mean correlation lengths and their standard deviations are very similar for the forecast error and bred vector, suggesting that the bred vector is able to provide information on the structure of the forecast error. The characteristic scale of error of the month is much shorter than what is currently used in the OI scheme (~1500 km). In addition, the fitted variance from the forecast error and bred vector both indicate larger amplitudes near the equator, particularly in the bred vector field. Here, we should note that the BV represents the structures of growing instability, and its magnitude is not to indicate the magnitude of the analysis/forecast error since we choose the rescaling breeding amplitude to be large enough to capture the growth of the ENSO-related coupled instability and to filter out the unwanted instabilities. The forecast errors appear as the result of analysis errors in the initial condition and the model deficiency so its variance is shown

TABLE 1. The error zonal correlation lengths and mean error variance of SST, obtained by fitting the bred vector and forecast error with a Gaussian function.

	Correlation length (km)		STD of correlation length (km)		Fitted variance (°C^2)	
	Forecast error	Bred vector	Forecast error	Bred vector	Forecast error	Bred vector
2.5°–7.5°N	514	540	272	269	0.63	0.05
2.5°S–2.5°N	575	505	251	226	0.99	0.14
7.5°–2.5°S	445	416	217	199	0.83	0.07

to be larger compared to BVs. Results also show that both the meridional correlation scales estimated from the forecast error and bred vector are similar to the one used in the current OI scheme (~400 km). In practical applications, it may not be easy to determine the correlation length in different regions every analysis cycle. Instead the full BV states can be used to augment the structures of the background error covariance in the data assimilation system (as discussed in section 1) and the augmented amplitude can be globally scaled to have the same amplitude as the 3DVARR/OI background error covariance (Yang et al. 2007).

c. *Dynamic error structure in the equatorial subsurface ocean*

In the previous subsections, we have shown that in the eastern Pacific both the growth of BV SST and the forecast error are dominated by similar dynamic errors. The growth of SST perturbations in the western Pacific is limited by its low natural variability due to the deep well-mixed surface warm water. As the result, the growth of temperature perturbations is less detectable near the surface layer in the western-central Pacific. However, *subsurface* perturbations can carry the information of coupled instabilities driven by the wind stress. Moreover, the warm pool in this region plays an essential role in the interaction between the atmosphere and the ocean through heat exchange at the surface. These observations suggest that a good ensemble forecast system for ENSO prediction should be able to generate perturbations to include the uncertainties related to these effects of covariabilities.

It has been recognized that interannual variability of equatorial subsurface temperature has large variance near the mean thermocline, that is, at a depth of about 175 m in the west Pacific and 50 m in the east. Figures 4a and 4b show that the first two leading EOF modes of the anomalous ocean subsurface temperature fields (computed using the vertical cross section of temperature analysis fields at the equator) are strongly related to the development of an ENSO event and explain more than 60% of the total variance of the equatorial subsurface temperature. The leading mode has large variability located in the eastern Pacific (mature El Niño) and its corresponding principal component is in phase with the variations of the Niño-3 index. The second mode, related to the early development of the event, exhibits large variability that extends from the

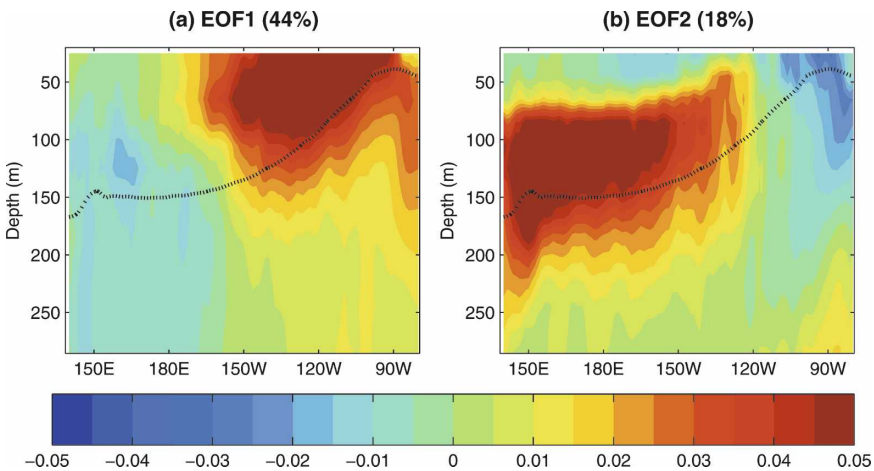

FIG. 4. (a) The first EOF mode of the equatorial temperature anomaly and (b) the second mode. The thick dashed line is the depth of the mean thermocline. EOF modes are normalized, and their explained variances are in parentheses.

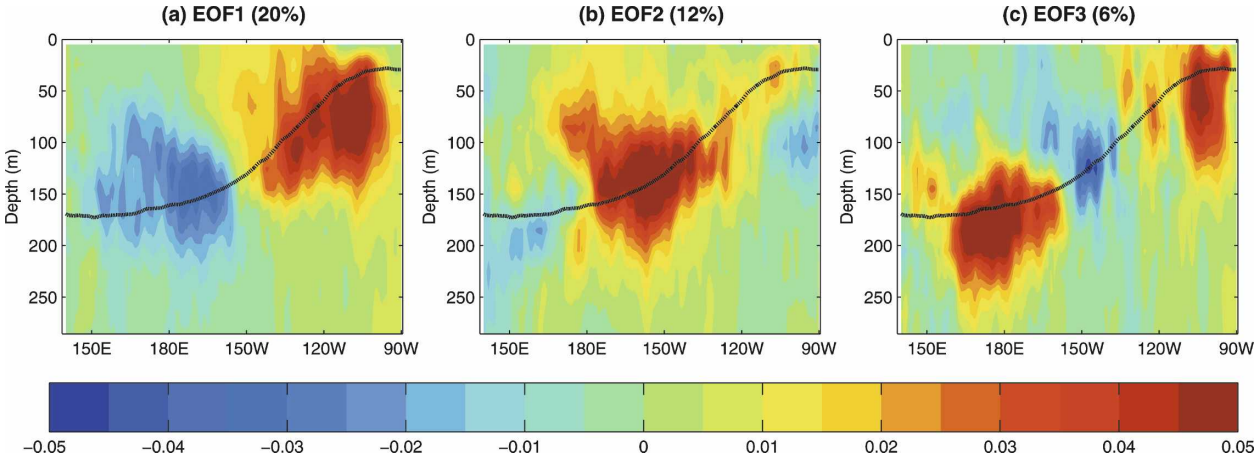

FIG. 5. As in Fig. 1, but for (a) the first EOF mode of equatorial temperature of forecast error, (b) the second mode, and (c) the third mode.

subsurface of the western Pacific and peaks in the central Pacific. Based on the temperature analysis fields, this mode leads the first one by about 7 months. It is clear that for ENSO prediction, the ability to describe thermal variations in subsurface conditions should strongly contribute to how well the SST forecast performs. The NASA GMAO CGCM exhibits reasonable interannual phase variations in the subsurface but the simulated subsurface temperature variations from this CGCM have a weak magnitude compared to the observations (not shown). Also, the current ensemble spread from operational ensemble perturbations is very limited near the thermocline in the western Pacific and smaller than the temperature error. Such a limitation due to the suboptimal ensemble perturbations and imperfect model physics is a common feature of many CGCMs and will crucially influence the ability to forecast SST anomalies in the equatorial eastern Pacific. Although BVs are not intended to capture the errors due to model deficiencies, they are used to reduce the initial errors associated to the corresponding initial atmospheric–oceanic conditions.

The same EOF analysis is applied to the forecast error and the bred vector temperature cross section at the equator. Figures 5a–c show the first three EOF modes of forecast error and their explained variances are 20%, 12%, and 6%, respectively. The first two modes of the forecast error have somewhat similar locations as the dominant ENSO-related modes, and they all show large amplitudes along the thermocline. The first mode has large variabilities in both the eastern and western Pacific with comparable amplitudes. The second mode is mainly located in the central Pacific. This implies that the subsurface growing error is dominated by large-scale variations, related to the zonal tilt of the thermocline. Comparing with Fig. 4, these patterns shown in Fig. 5 strongly project on the space of ENSO-related variability. Consequently, such growing errors will develop variations like El Niño–La Niña.

We then applied the same EOF analysis to the bred vector equatorial temperature. Here, we use the bred vectors before rescaling, that is, the bred vectors are weighted by their growth rates, in order to find the patterns that dominate the growing components. Figures 6a–c show the first three EOF modes and have similar amounts of explained variances (7%, 8%, and 9%). The EOF modes have a striking resemblance to the EOF modes of the forecast error. Here the ordering of the BV's EOF mode is rearranged in order for convenient comparison and to emphasize their relation with the forecast error. As discussed before, the relatively low explained variances should not be a serious concern for our understanding and for implication. The results are obtained from the fact that, in addition to ENSO instabilities, there are also other instabilities and processes with very different space and time scales present in such a complex system (i.e., very large degrees of freedom). Despite this, the dominant growing pattern is still associated with the large-scale variations. This supports the hypothesis that bred vectors can capture the shape of the related dynamic error that dominates the forecast error. Currently, the background error covariance in the univariate optimal interpolation analysis uses a Gaussian shape in the horizontal and vertical directions. By contrast, the patterns of EOF modes suggest that the background error in the subsurface should have considered large-scale shapes expanding near the thermocline in order to ensure the corrections from the data assimilation scheme project on the ENSO-related low dimensional space.

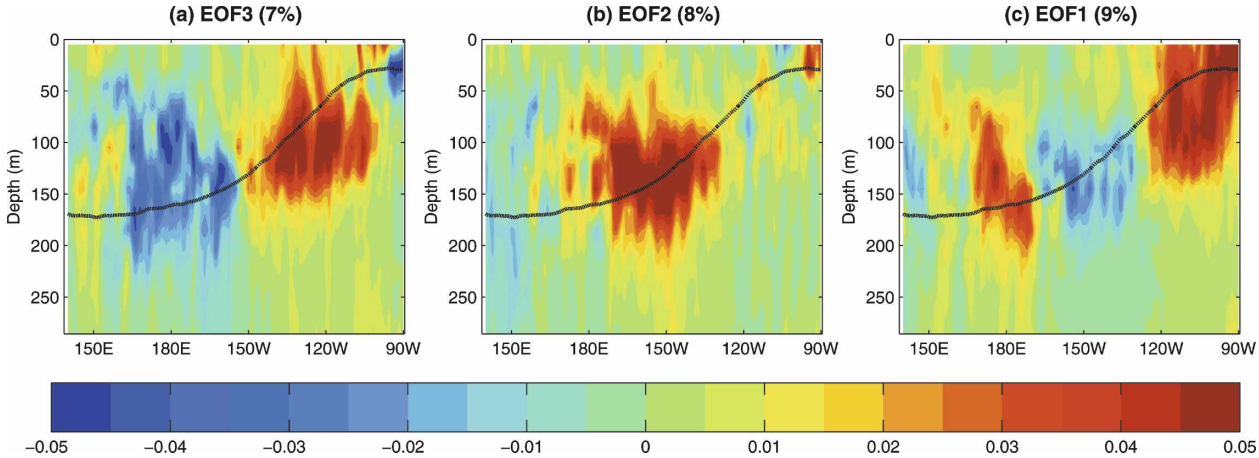

FIG. 6. As in Fig. 1, but for (a) the third EOF mode of equatorial temperature of the unrescaled bred vector, (b) the second mode, and (c) the first mode.

We also notice that in the BV EOF modes, there is a feature locally trapped in the extreme eastern equatorial Pacific near surface. This feature is absent in the EOF modes of the forecast error. This may be due to the rapid dynamical adjustment of Ekman pumping in the shallow region off the South American coast when adding the bred perturbation to the unperturbed control background, that is, the analysis field.

4. Application to ensemble forecasting: Case study for 1997/98 El Niño

To explore the impact of using coupled BV for ensemble forecasting, we performed a two-sided breeding cycle (Toth and Kalnay 1997) to generate initial ensemble perturbations and study the impact on predictions of the strong 1997/98 El Niño event. In a two-sided breeding cycle, pairs of positive and negative bred perturbations are used to perturb the initial state. The rescaling factor is then measured by the difference between this pair of perturbations after one month, calculated according to Eq. (1):

$$\text{factor} = \frac{\|\delta x_0\|}{\|\delta x(t)\|} = \frac{\|\delta x_0\|}{\|0.5 \times [x_p(t) - x_n(t)]\|}. \qquad (1)$$

In Eq. (1), $\|\delta x_0\|$ is the initial size of the perturbation (e.g., the rms of Niño-3 BV SST chosen to be 0.1°C) and $\|\delta x(t)\|$ is the evolved (unrescaled) bred perturbation after one month, $x_p(t)$ is the positively perturbed one-month forecast and $x_n(t)$ is the negatively perturbed one-month forecast. This constant factor is then applied to rescale the evolved bred perturbation. This rescaled perturbation is added and subtracted from the control as the next initial condition for the next breeding cycle.

Studies have shown that the trigger and development of this event is closely related to a series of westerly wind bursts with long fetch along the equator, which weakened and reversed the trade winds in early 1997 (McPhaden 1999). The wind burst forced a downwelling Kelvin wave that deepened the thermocline in the eastern equatorial Pacific and contributed to the development of the warm SST anomaly. The reduced zonal SST gradient helped to strengthen the westerly wind anomalies. The anomalous states were further intensified due to the nonlinear interactions between the atmosphere–ocean coupling, including phase locking with the seasonal variability in the equatorial Pacific.

The hindcast experiment with the operational ensemble is able to predict the phase and intensity of this event after it has already developed (e.g., starting on May 1997). The hindcast initialized in January 1997 forecasts a warm event, but underestimates the intensity. Using forecasts started from a pair of positive and negative BV perturbations, we found that the mean from this pair of ensemble members is able to substantially improve upon the control (unperturbed) forecast starting from January 1997. In the following analysis, we use this case to discuss the impact of applying coupled BV perturbations.

Starting from January 1997, we found that the ensemble member initialized with the positive BV captures very well the intensity of this strong El Niño event and that the anomalous phase is more accurate, as shown by the red line in Fig. 7. The observed Niño-3 index (the blue dashed line) is computed from the Reynolds SST and is used for verification. The forecast initialized with the negative BV (red dashed–dotted line) shows a behavior rather similar to that of the control forecast (black line). For convenience, we will refer to the positive BV as PBV, and the negative BV as

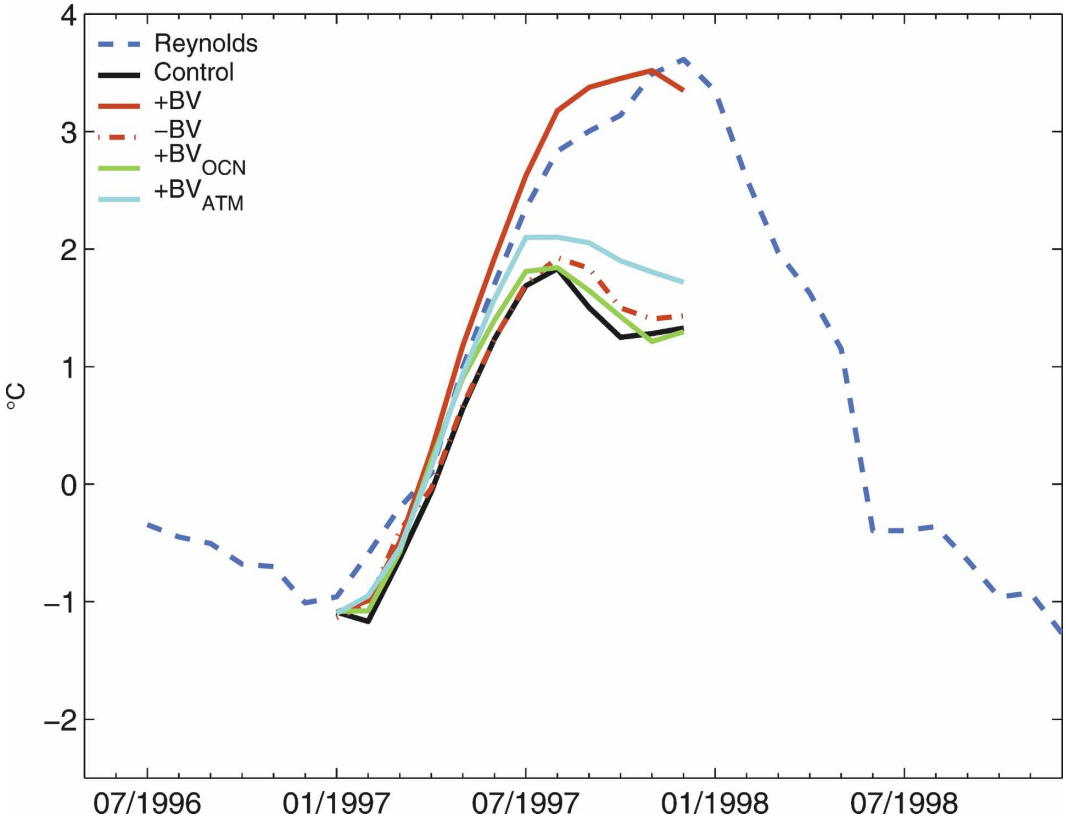

FIG. 7. Forecast Niño-3 indices from different initial condition starting from January 1997. The observed Niño-3 index (from Reynolds SST) is denoted with a blue dashed line. The control forecast without perturbation is denoted as the black line. The red solid line is the forecast initialized with PBV, the red dot–dash line is the one initialized with NBV, the green solid line is the one initialized with perturbed ocean only from PBV, and the cyan line is the one initialized with perturbed atmosphere only from PBV. See the detailed discussion in section 4a.

NBV and the control forecast as CNT. To test whether the best forecast in this case can only be achieved when both the atmosphere and ocean are perturbed, we performed two additional forecast experiments that use only the ocean component of the PBV as the initial perturbation (PBVO) and only the atmospheric component (PBVA). Neither PBVO (the green line) nor PBVA (the magenta line) are able to reproduce the intensity of the anomalous warm state that PBV predicted, even though PBVA shows a larger impact than perturbing the ocean alone. Our results suggest that only when the coupled bred perturbation is applied is the evolved perturbation able to maximize the coupling effect and predict the event.

The initial SST perturbation of PBV at this time, shown in Fig. 8a, has a warm perturbation located in the eastern Pacific (140°–100°W) and a slight cool perturbation in the west. The bred temperature perturbation in the subsurface reflects the downwelling/deepening perturbation of the thermocline in the eastern Pacific (Fig. 8b). On the western edge of the warm perturbations, there are corresponding westerly wind perturbations in the equatorial central Pacific. As we will discuss later, the westerly wind perturbation is able to expand farther to the east and makes the downwelling (deepening) effect more easily amplified in the shallow region. Although the details of the appearance of the wind burst in PBV are not completely consistent with observations, the development of the warm anomaly in PBV has a similar triggering effect and results in a better prediction of the strong El Niño event.

We examine the Hovmoeller diagram of zonal wind stress from these experiments and notice that only PBV (Fig. 9b) has the westerly wind burst that took place in mid-February until early March, slightly earlier than the observations (Fig. 9f). Also, the duration of this wind burst in Fig. 9b is long and it extends to 140°W, while other forecast members show relatively neutral or easterly wind anomalies during March. In addition, only PBV shows the consistent strong positive wind anomaly after the El Niño event has been established in May 1997, suggesting its role is tightly coupled with the

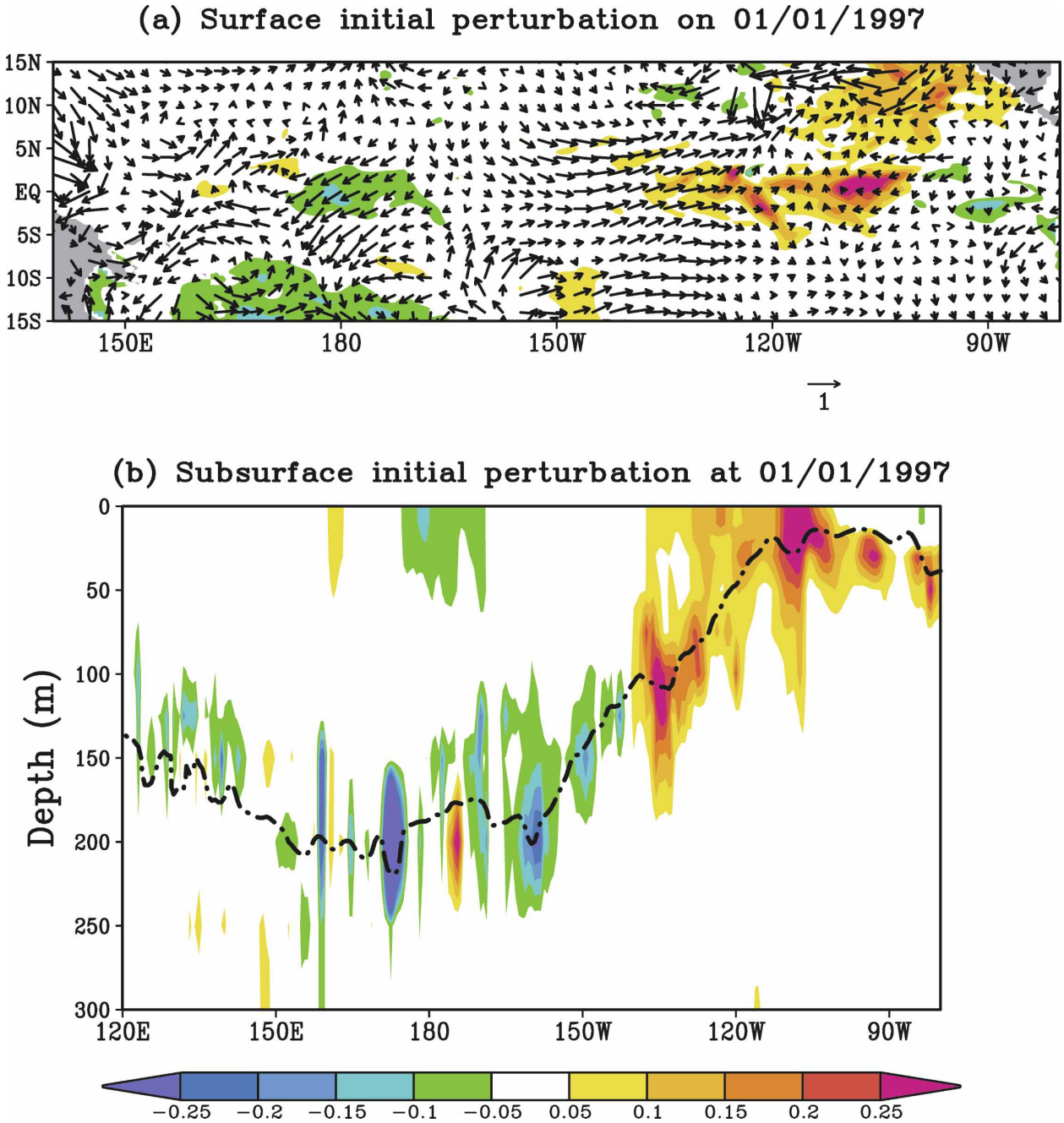

FIG. 8. Bred perturbation used to initialize PBV: (a) SST perturbation (°C) with color shading and wind perturbation (m s^{-1}), shown as vector, averaged from 1000 to 850 hPa, and (b) the temperature perturbation along the equator with the dash–dotted line denoting the depth of the background 20°C isotherm.

warm anomaly in the upper ocean. This can also be observed in the anomalous changes of the subsurface structure. The similar response in the low-frequency variability between the PBV and the observation, although they differ in detail, suggests that successful predictions of the 1997 El Niño event do not rely on deterministic variations only. The result may relate to linear stochastic forcing theory of ENSO (Zavala-Garay et al. 2005). The atmospheric perturbation of PBV projects on the low-frequency variations and together with the oceanic perturbation induces a stronger ENSO response.

Figure 10 shows the monthly mean vertical temperature in the equatorial upper ocean above 300 m. The

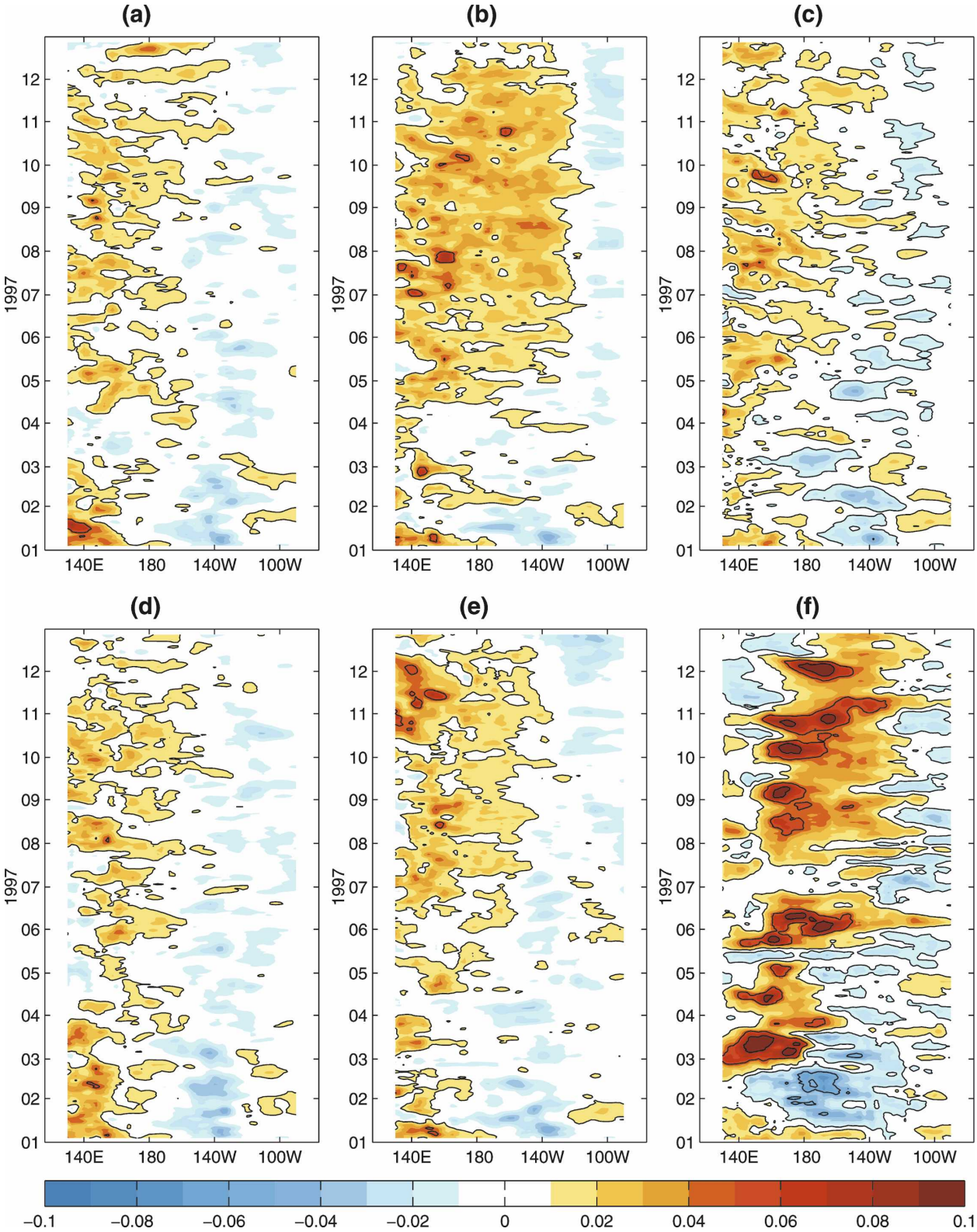

FIG. 9. Forecast zonal wind stress anomaly (N m^{-2}) over the ocean from January 1997 to December 1997 from (a) the control forecast, (b) the perturbed forecast initialized with the PBV, (c) the perturbed forecast initialized with the NBV, (d) the perturbed forecast initialized with the PBVO (ocean only), (e) the perturbed forecast initialized with the PBVA (atmosphere only), and (f) observations, obtained from SSM/I. All fields are daily data with a 1-week running mean.

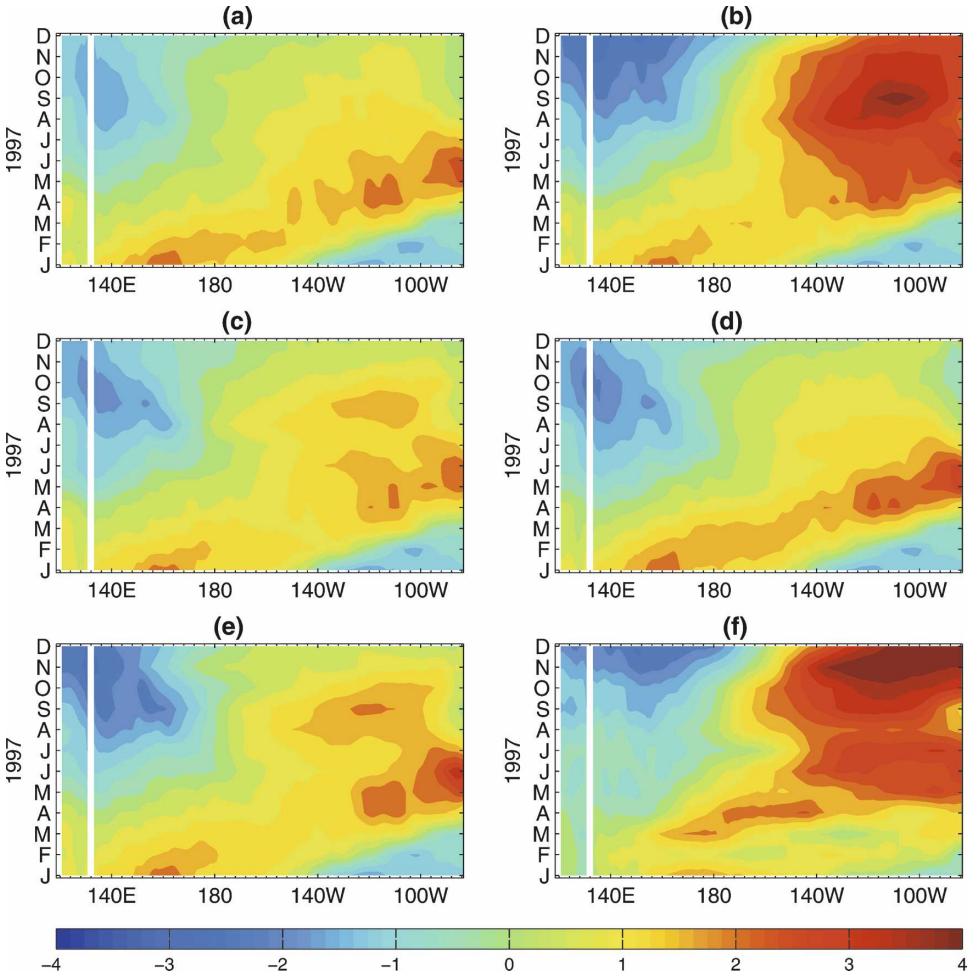

FIG. 10. Monthly mean equatorial vertically average temperature anomaly (°C) in the upper ocean (defined as the upper 300 m) from January 1997 to December 1997 from (a) the control forecast, (b) the perturbed forecast initialized with the PBV, (c) the perturbed forecast initialized with the NBV, (d) the perturbed forecast initialized with the PBVO (ocean only), and (e) the perturbed forecast initialized with the PBVA (atmosphere only), and (f) the analysis data. The analysis data used for validation are derived from the OI scheme implemented in the same ocean GCM, assimilating temperature and synthetic salinity profiles.

analysis state derived from the data assimilation scheme is used to represent the best estimate of the true state. As shown in Fig. 10a, a seesaw pattern (negative–positive anomaly to represent the flattened thermocline) is evident during the intensification of this warm event because of the positive feedback from air–sea interaction. Overall, the source of the forecast skill from all the ensembles is the subsurface western Pacific, where all the forecast states have already indicated a deepening anomaly and are able to describe its eastward propagation. However, only PBV captures the dominant seesaw pattern in the subsurface temperature anomaly, though the mature phase is about one month ahead of the verification. In the early forecast months, all of the forecast states (including PBV) show a too-shallow thermocline in the eastern basin and they stay in the cold phase. Such results indicate that a much better depiction of the equatorial wave propagations could be obtained if the perturbation is able to effectively modulate the wind forcing. In addition, except for PBV, the amplitude of the deepening anomaly decays prematurely and the deepening feature near the eastern end of the Pacific basin becomes neutral after September.

We notice that when the PBV atmospheric component is used (PBVA), it has some important features shown in PBV. For example, the deepening feature is able to develop in the eastern Pacific even though the amplitude is smaller, and it includes the shoaling anomaly in the western Pacific. This is evidence that the

atmospheric perturbation carries information that is able to drive the tilting of the thermocline.

5. Summary and discussion

The coupled breeding method has been implemented into the NASA GMAO operational coupled GCM, in which the ocean component assimilates the real temperature observations through an OI scheme. Breeding experiments are then performed under this imperfect model scenario, so that growing errors are much more complicated than in the perfect model scenario explored in Yang et al. (2006). They include, in addition to those dominated by the coupled ENSO dynamics, other errors such as initial errors due to an imperfect data assimilation scheme, noisy observation errors, and model errors (as well as those due to the spinup of the AMIP atmospheric initialization). We explore the possibility that bred vectors could still be used as a proxy to represent the structure of the one-month forecast errors despite the presence of these complications in a real operational system. Potential applications for this work are the improvement of ENSO ensemble forecasting system and the better use of observations in the data assimilation scheme by including evolving "errors of the month."

For the ENSO prediction, the forecast SST in the tropical Pacific is the most crucial variable directly depicting air–sea interaction and determining the performance of the coupled GCM. As a first step, we analyze the temperature structure characteristics of the one-month forecast errors and the bred vectors. One-month forecast errors show dynamical structures evolving with the variations of the background flow and bred vectors strongly project onto these forecast errors. Both the amplitude of forecast error and the bred vector growth rate are dominated by low-frequency variations with a very similar trend: they are small when the background anomalies are in the mature phase of ENSO events and are large when the background anomalies are near neutral, especially during the sharp transition that occurred from the 1997/98 strong El Niño to the 1999 La Niña event. A statistical analysis suggests that the agreement between bred vector and forecast error is particularly good when the BV growth rate is large and when the background anomaly is near neutral. In addition, our results suggest that the leading EOF modes of subsurface structure of one-month forecast errors and bred vectors are both dominated by similar large-scale features with peak variations near the thermocline.

For the 1997 El Niño event, the forecast error of the temperature cross section along the equator shows that large error appeared first in the subsurface of the central-to-western Pacific, propagated eastward, and amplified off the east coast during the development of this strong event. The operational forecast error is smallest near the surface at the mature stage but the subsurface errors show a wide zonal expansion. The evolution of the one-month subsurface forecast error structure shows that the errors reflect the large-scale displacement of the thermocline associated with the anomalous background variations. The bred vectors at the relevant times captured most of the shapes of the one-month forecast error, including the eastward propagation and vertical and zonal expansion, even though they were computed without using observations.

The potential application of using bred vectors in the ocean data assimilation is also explored in this study. For a complex system like a coupled GCM, it is far too costly and practically impossible to retrieve the full dimension, atmosphere–ocean error covariance structure. However, it is possible to create a shortcut, representing the dominant structures with the bred vectors derived here to augment the time-independent covariance structure. We have demonstrated that bred vectors are characterized by similar correlation length as the ones derived from the forecast error, even though the bred vector is calculated only from the difference between perturbed and unperturbed forecasts and has no information about the analysis used to calculate the forecast errors. The horizontal correlation length associated with "errors of the month" is found to be shorter than the one used in OI scheme.

Last, we include the coupled bred vectors with two-sided breeding in the ensemble members to explore the impact of using coupled initial perturbations. Our results show that the mean from the pair of BV ensemble members substantially improves the control forecast starting from January 1997 because one of the BV members captures most of the important features in the 1997/98 El Niño event. We found that such a result cannot be achieved if only the atmospheric or the oceanic component of the bred perturbation is retained. Only when the coupled perturbation is used are the amplitude and phase of the forecasted warm event close to the observed evolution. The successful member initialized with the positive BV is the only one that developed westerly wind bursts that extended eastward of the date line in early 1997 and suggest it captures the most probable coupled uncertainties. We believe this precursor contributes to the subsequent well-developed positive feedback of this event, including the deepening thermocline in the eastern Pacific and the consistent positive zonal wind stress anomaly that prevailed in the central basin.

For the next phase of our studies, we will extend the

coupled bred vectors with two-sided breeding in the ensemble members for a much longer hindcast experiment period so that we can explore their impact on different starting months. Additionally, based on our results of error structure in subsurface temperature, we will explore the possibility of including the time-varying error structures derived from the BV in the background error covariance within a data assimilation scheme like OI. By using such dynamically related error covariance, the corrections made to the background state with the observation information are expected to reflect the anomalous, flow-dependent variations in the subsurface.

Currently, the NASA ensemble Kalman filter (EnKF), developed for the purpose of ocean data assimilation (Keppenne and Rienecker 2002), typically has an analysis interval of 5 days in this NASA system. So the ensemble members used to construct the flow-dependent background errors covariance are dominated by the oceanic instabilities and may not correct the background errors projecting onto the coupled instabilities. Moreover, the EnKF can suffer from ensemble collapse and may not span the range of uncertainties associated with the dominant coupled modes. The underestimation of the ensemble forecast spread due to the absence of some unstable directions and the neglect of model errors in the formulation of the system noise can result in overconfidence in the forecast (ensemble collapse) during the process of data assimilation. Although procedures like multiplicative and additive variance inflation (Anderson and Anderson 1999; Hamill and Whitaker 2005) commonly used in EnKF-based schemes can alleviate such problem, we suggest that augmenting the ensemble members from the EnKF with the BVs in order to capture the most important coupled growing directions would allow errors to project on the low-frequency variations. Therefore, it is possible to provide a better background error covariance after BVs are incorporated in the EnKF framework.

For the applications on the numerical weather prediction (NWP), Corazza et al. (2003, 2007) and Yang et al. (2007) show that refreshing the bred structures by adding a small amount of random perturbations during the breeding cycles is able to efficiently prevent the bred ensemble collapsing into similar directions. This method is also akin to the additive perturbation used in EnKF and allows the bred vectors to capture more growing directions. In future applications on ensemble forecasting or data assimilation, we may need more ensemble members to describe the subgrowing directions, but this can also be approached with a similar idea discussed above and by including random perturbation (white noise like) wind fields in the monthly breeding cycle. However, the question raised here may be somewhat different from the point view of NWP since the interannual instability is dominated by the ENSO variability depending on the longer memory of the ocean component. Therefore, it is reasonable to assume that the coupled bred vectors are associated with the growth of the slowly varying ENSO-related instability. We also note that for the slow coupled ENSO bred vectors, the presence of weather is a large source of noise, which should accomplish the same effect of refreshing the bred vectors. Therefore, though the coupled bred vectors are dominated by similar slowly varying instability, their structure will not be too similar and can be reasonably used to augment the background error covariance in the data assimilation.

Acknowledgments. We are very grateful for much technical support from NASA GMAO support staff, especially to Sonya Miller. We also greatly appreciate many valuable discussions with Joaquim Ballabrera. The University of Maryland component of this work has been supported by grants from the NASA Seasonal-to-Interannual Prediction Project (NASA-NAG-55825 and NASA-NAG-12418). The GMAO component of this work has been supported by the Modeling, Analysis, and Prediction program under RTOP 622-24-47 and WBS 802678.02.12.

APPENDIX A

Fitting the Forecast Error/Bred Vector with a Gaussian Function

In this section, we briefly describe the procedures that we use to obtain the fitting parameters of a Gaussian function, that is, the fitted error variance (C_0) and the correlation length (L) in Eq. (A1):

$$f(r) = C_0 \exp\left(-\frac{r^2}{L^2}\right). \tag{A1}$$

The Levenberg–Marquardt algorithm is first applied to estimate these parameters, and the standard deviation corresponding to the fitting points are required for nonlinear fitting. In our results, the standard deviations from both the one-month forecast error and bred vector have larger values at short ranges and smaller values near the tail. Therefore, this scheme will try to overfit the tail. To avoid overemphasizing the small covariances at large separations (which is dominated by sampling errors), we use the e-folding value of the average of the first two fitting points to determine how many

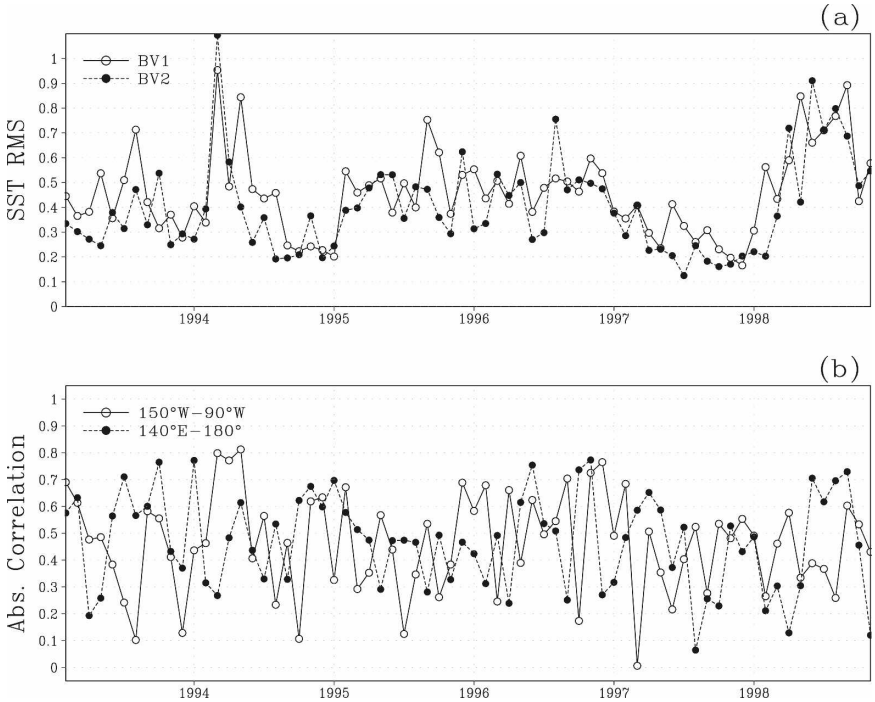

FIG. B1. (a) The rms of BV1 and BV2 SST (°C) in the Niño-3 region and (b) the absolute value of the spatial correlation between BV1 and BV2 SST in the eastern Pacific (Niño-3 region, i.e., 5°N–5°S, 150°–90°W) and in the western Pacific (5°N–5°S, 140°E–180°).

data points should be used for fitting, and a corresponding length, L_e, is chosen.

Once (C_0, L) are determined, we repeat the procedure by increasing the number of points used for the fitting and calculate the rms error within L_e. The (C_0, L), which has the smallest rms error, is assigned to our final result. If the e-folding range cannot be found at the last point of the data, it suggests a very large-scale linear behavior of the error covariance. We then switch to a simple linear regression form [Eq. (A2)] to avoid failure in fitting the nonlinear scheme:

$$\ln[f(r)] = \ln C_0 - \frac{r^2}{L^2}. \tag{A2}$$

APPENDIX B

Bred Vectors with Different Rescaling Norms

In this section, we will compare BVs derived from two different rescaling norms: 1) the BV SST in the Niño-3 region with an amplitude of 0.1°C and 2) the BV D20 (the depth of 20° isotherm) in the tropical Pacific with an amplitude of 0.2 m, and both are rescaled every month. They are referred as to BV1 and BV2, and the results shown in section 3 are related to BV1. In addition, with one-month rescaling period, it is long enough to capture the growth of the slowly varying instability associated with ENSO. We also found that BVs' structures are dominated by similar growing instabilities but are not identical due to the nonlinearity of the coupled system.

Figure B1a is the time series of the RMS of the BV1 and BV2 SST (unrescaled) in the Niño-3 region. The high correlation (0.67) between these two time series suggests similar growing structures in the Niño-3 region. The structures between these two BVs are compared in the eastern Pacific (Niño-3 region) and the western Pacific by computing their correlations. Figure B1b shows that overall the correlation is large in either region for the same month, which suggest that these two BVs have similar structures propagating in the tropical Pacific. The EOF analysis of BV2 has similar subsurface features as shown in Fig. 6 (not shown). These results confirm that BVs' structures are not sensitive to the rescaling norm as long as the rescaling period is long enough and the amplitude is reasonable to capture the growth of the coupled instabilities.

REFERENCES

Anderson, J. L., and S. L. Anderson, 1999: A Monte Carlo implementation of the nonlinear filtering problem to produce ensemble assimilations and forecasts. *Mon. Wea. Rev.,* **127,** 2741–2758.

Bacmeister, J. T., and M. J. Suarez, 2002: Wind stress simulations and the equatorial momentum budget in an AGCM. *J. Atmos. Sci.,* **59,** 3051–3073.

——, P. J. Pegion, S. D. Schubert, and M. J. Suarez, 2000: An atlas of seasonal means simulated by the NSIPP-1 atmospheric GCM. NASA Tech. Memo. 104606, Vol. 17, 194 pp.

Bengtsson, L., U. Schlese, E. Roeckner, M. Latif, T. P. Barnett, and N. Graham, 1993: A two-tiered approach to long-range climate forecasting. *Science,* **261,** 1026–1029.

Bergman, J. W., H. H. Hendon, and K. M. Weickmann, 2001: Intraseasonal air–sea interactions at the onset of El Niño. *J. Climate,* **14,** 1702–1719.

Boulanger, J.-P., and C. Menkes, 1995: Propagation and reflection of long equatorial waves in the Pacific Ocean during the 1991–1993 El Niño. *J. Geophys. Res.,* **100,** 25 041–25 059.

Buehner, M., 2005: Ensemble-derived stationary and flow-dependent background-error covariances: Evaluation in a quasi-operational NWP setting. *Quart. J. Roy. Meteor. Soc.,* **131,** 1013–1043.

Cai, M., E. Kalnay, and Z. Toth, 2003: Bred vectors of the Zebiak–Cane model and their application to ENSO predictions. *J. Climate,* **16,** 40–56.

Chang, P., L. Ji, H. Li, and M. Flügel, 1996: Chaotic dynamics versus stochastic processes in El Niño–Southern Oscillation in coupled ocean–atmosphere models. *Physica D,* **98,** 301–320.

Chen, D., M. A. Cane, A. Kaplan, S. E. Zebiak, and D. Huang, 2004: Predictability of El Niño over the past 148 years. *Nature,* **428,** 733–736.

Chen, Y.-Q., D. S. Battisti, T. N. Palmer, J. Barsugli, and E. S. Sarachik, 1997: A study of the predictability of tropical Pacific SST in a coupled atmosphere–ocean model using singular vector analysis: The role of the annual cycle and the ENSO cycle. *Mon. Wea. Rev.,* **125,** 831–845.

Corazza, M., and Coauthors, 2003: Use of the breeding technique to estimate the structure of the analysis "errors of the day." *Nonlinear Processes Geophys.,* **10,** 233–243.

——, E. Kalnay, and S. C. Yang, 2007: An implementation of the Local Ensemble Kalman Filter in a quasi geostrophic model and comparison with 3D-Var. *Nonlinear Processes Geophys.,* **14,** 89–101.

Evensen, G., 2003: The ensemble Kalman filter: Theoretical formulation and practical implementation. *Ocean Dyn.,* **53,** 343–367.

Fan, Y., M. R. Allen, D. L. T. Anderson, and M. A. Balmaseda, 2000: How predictability depends on the nature of uncertainty in initial conditions in a coupled model of ENSO. *J. Climate,* **13,** 3298–3313.

Fedorov, A., S. Harper, S. Philander, B. Winter, and A. Wittenberg, 2003: How predictable is El Niño? *Bull. Amer. Meteor. Soc.,* **84,** 911–919.

Galanti, E., E. Tziperman, M. Harrison, A. Rosati, R. Giering, and Z. Sirkes, 2002: The equatorial thermocline outcropping—A seasonal control on the tropical Pacific Ocean–atmosphere instability strength. *J. Climate,* **15,** 2721–2739.

Gates, W. L., 1992: AMIP: The Atmospheric Model Intercomparison Project. *Bull. Amer. Meteor. Soc.,* **73,** 1962–1970.

Hamill, T. M., and J. S. Whitaker, 2005: Accounting for the error due to unresolved scales in ensemble data assimilation: A comparison of different approaches. *Mon. Wea. Rev.,* **133,** 3132–3147.

Hayes, S. P., L. J. Mangum, J. Picaut, A. Sumi, and K. Takeuchi, 1991: TOGA-TAO: A moored array for real-time measurements in the tropical Pacific Ocean. *Bull. Amer. Meteor. Soc.,* **72,** 339–347.

Ji, M., and A. Leetmaa, 1997: Impact of data assimilation on ocean initialization and El Niño prediction. *Mon. Wea. Rev.,* **125,** 742–753.

Keppenne, C. L., and M. M. Rienecker, 2002: Initial testing of a massively parallel ensemble Kalman filter with the Poseidon isopycnal ocean general circulation model. *Mon. Wea. Rev.,* **130,** 2951–2965.

——, and ——, 2003: Assimilation of temperature into an isopycnal ocean general circulation model using a parallel ensemble Kalman filter. *J. Mar. Syst.,* **40–41,** 363–380.

——, ——, N. P. Kurkowski, and D. D. Adamec, 2005: Ensemble Kalman filter assimilation of temperature and altimeter data with bias correction and application to seasonal prediction. *Nonlinear Processes Geophys.,* **12,** 491–503.

Kirtman, B. P., 2003: The COLA anomaly coupled model: Ensemble ENSO prediction. *Mon. Wea. Rev.,* **131,** 2324–2341.

Kleeman, R., Y. Tang, and A. Moore, 2003: The calculation of climatically relevant singular vectors in the presence of weather noise as applied to the ENSO problem. *J. Atmos. Sci.,* **60,** 2856–2867.

Koster, R. D., and M. J. Suarez, 1992: Modeling the land surface boundary in climate models as a composite of independent vegetation stands. *J. Geophys. Res.,* **97,** 2697–2715.

Latif, M., A. Sterl, E. Maier-Reimer, and M. M. Junge, 1993: Structure and predictability of the El Niño/Southern Oscillation phenomenon in a coupled ocean–atmosphere general circulation model. *J. Climate,* **6,** 700–708.

Lorenc, A. C., 2003: The potential of the ensemble Kalman filter for NWP: A comparison with 4D-VAR. *Quart. J. Roy. Meteor. Soc.,* **129,** 3183–3203.

McPhaden, M. J., 1999: Equatorial waves and the 1997–98 El Niño. *Science,* **283,** 950–954.

——, and X. Yu, 1999: Genesis and evolution of the 1997–98 El Niño. *Geophys. Res. Lett.,* **26,** 2961–2964.

——, and Coauthors, 1998: The tropical ocean–global atmosphere observing system: A decade of progress. *J. Geophys. Res.,* **103,** 14 169–14 240.

Moore, A. M., and R. Kleeman, 1996: The dynamics of error growth and predictability in a coupled model of ENSO. *Quart. J. Roy. Meteor. Soc.,* **122,** 1405–1446.

——, and ——, 1997a: The singular vectors of a coupled ocean–atmosphere model of ENSO. I: Thermodynamics, energetics, and error growth. *Quart. J. Roy. Meteor. Soc.,* **123,** 953–981.

——, and ——, 1997b: The singular vectors of a coupled ocean–atmosphere model of ENSO. II: Sensitivity studies and dynamical interpretation. *Quart. J. Roy. Meteor. Soc.,* **123,** 983–1006.

——, and ——, 1998: Skill assessment for ENSO using ensemble prediction. *Quart. J. Roy. Meteor. Soc.,* **124,** 557–584.

Palmer, T. N., and Coauthors, 2004: Development of a European Multimodel Ensemble System for Seasonal-to-Interannual Prediction (DEMETER). *Bull. Amer. Meteor. Soc.,* **85,** 853–872.

Peña, M., and E. Kalnay, 2004: Separating fast and slow modes in coupled chaotic systems. *Nonlinear Processes Geophys.,* **11,** 319–327.

Peng, P., Q. Zhang, A. Kumar, H. van den Dool, W. Wang, S. Saha, and H. Pan, 2004: Variability, predictability and prediction of DJF climate in NCEP coupled forecast system. *Proc. 29th Climate Prediction and Diagnostic Workshop,* Madison, WI, National Weather Service. [Available online at

http://www.cpc.noaa.gov/products/outreach/proceedings/cdw29_proceedings/Peng.pdf.]

Reynolds, R. W., N. A. Rayner, T. M. Smith, D. C. Stokes, and W. Wang, 2002: An improved in situ and satellite SST analysis for climate. *J. Climate,* **15,** 1609–1625.

Rosati, A., K. Miyakoda, and R. Gudgel, 1997: The impact of ocean initial conditions on ENSO forecasting with a coupled model. *Mon. Wea. Rev.,* **125,** 754–772.

Saha, S., and Coauthors, 2006: The NCEP Climate Forecast System. *J. Climate,* **19,** 3483–3517.

Schneider, E., B. Huang, Z. Zhu, D. DeWitt, J. Kinter III, B. Kirtman, and J. Shukla, 1999: Ocean data assimilation, initialization, and predictions of ENSO with a coupled GCM. *Mon. Wea. Rev.,* **127,** 1187–1207.

Schopf, P., and A. Loughe, 1995: A reduced-gravity isopycnal ocean model: Hindcasts of El Niño. *Mon. Wea. Rev.,* **123,** 2839–2863.

Slingo, J. M., D. P. Rowell, K. R. Sperber, and F. Nortley, 1999: On the predictability of the interannual behaviour of the Madden–Julian oscillation and its relationship with El Niño. *Quart. J. Roy. Meteor. Soc.,* **125,** 583–609.

Stockdale, T. N., D. L. T. Anderson, J. O. S. Alves, and M. A. Balmaseda, 1998: Global seasonal rainfall forecasts using a coupled ocean–atmosphere model. *Nature,* **392,** 370–373.

Takacs, L. L., and M. J. Suarez, 1996: Dynamical aspects of climate simulations using the GEOS general circulation model. NASA Tech. Memo. 104606, Vol. 10, 76 pp.

Tang, Y., R. Kleeman, and S. Miller, 2006: ENSO predictability of a fully coupled GCM model using singular vector analysis. *J. Climate,* **19,** 3361–3377.

Toth, Z., and E. Kalnay, 1993: Ensemble forecasting at NMC: The generation of perturbations. *Bull. Amer. Meteor. Soc.,* **74,** 2317–2330.

——, and ——, 1996: Climate ensemble forecasts: How to create them? *Idojaras,* **100,** 43–52.

——, and ——, 1997: Ensemble forecasting at NCEP and the breeding method. *Mon. Wea. Rev.,* **125,** 3297–3319.

Troccoli, A., and K. Haines, 1999: Use of the temperature–salinity relation in a data assimilation context. *J. Atmos. Oceanic Technol.,* **16,** 2011–2025.

——, M. M. Rienecker, C. L. Keppenne, and G. C. Johnson, 2003: Temperature data assimilation with salinity corrections: Validations for the NSIPP ocean data assimilation system in the tropical Pacific Ocean, 1993–1998. NASA Tech. Memo. 2003-104606, Vol. 24, 23 pp.

Vecchi, G. A., A. T. Wittenberg, and A. Rosati, 2006: Reassessing the role of stochastic forcing in the 1997–1998 El Niño. *Geophys. Res. Lett.,* **33,** L01706, doi:10.1029/2005GL024738.

Vialard, J., F. Vitart, M. A. Balmaseda, T. N. Stockdale, and D. L. Anderson, 2003a: An ensemble generation method for seasonal forecasting with an ocean–atmosphere coupled model. ECMWF Tech. Memo. 417, 20 pp.

——, A. T. Weaver, D. L. T. Anderson, and P. Delecluse, 2003b: Three- and four-dimensional variational assimilation with a general circulation model of the tropical Pacific Ocean. Part II: Physical validation. *Mon. Wea. Rev.,* **131,** 1379–1395.

Vikhliaev, Y., B. Kirtman, and P. Schopf, 2007: Decadal North Pacific bred vectors in a coupled GCM. *J. Climate,* **20,** 5744–5764.

Vintzileos, A., M. M. Rienecker, M. J. Suarez, S. K. Miller, P. J. Pegion, and J. T. Bacmeister, 2003: Simulation of the El Niño–Interannual Prediction Project coupled general circulation model. *CLIVAR Exchanges,* Vol. 8, International CLIVAR Project Office, Southampton, United Kingdom, 25–27.

Wallace, J. M., E. M. Rasmusson, T. P. Mitchell, V. E. Kousky, E. Sarachik, and H. von Storch, 1998: On the structure and evolution of ENSO-related climate variability in the tropical Pacific: Lessons from TOGA. *J. Geophys. Res.,* **103,** 14 241–14 260.

Wang, X., C. Snyder, and T. M. Hamill, 2007: On the theoretical equivalence of differently proposed ensemble–3DVar hybrid analysis schemes. *Mon. Wea. Rev.,* **135,** 222–227.

Weaver, A. T., J. Vialard, and D. L. T. Anderson, 2003: Three- and four-dimensional variational assimilation with a general circulation model of the tropical Pacific Ocean. Part I: Formulation, internal diagnostics, and consistency checks. *Mon. Wea. Rev.,* **131,** 1360–1378.

Xue, Y., M. A. Cane, S. E. Zebiak, and M. B. Blumenthal, 1994: On the prediction of ENSO: A study with a low order Markov model. *Tellus,* **46A,** 512–528.

Yang, S., K. Lau, and P. Schopf, 1999: Sensitivity of the tropical Pacific Ocean to precipitation induced freshwater flux. *Climate Dyn.,* **15,** 737–750.

Yang, S.-C., M. Cai, E. Kalnay, M. Rienecker, G. Yuan, and Z. Toth, 2006: ENSO bred vectors in coupled ocean–atmosphere general circulation models. *J. Climate,* **19,** 1422–1436.

Zavala-Garay, J., C. Zhang, A. M. Moore, and R. Kleeman, 2005: The linear response of ENSO to the Madden–Julian oscillation. *J. Climate,* **18,** 2441–2459.

Zhang, X., and M. J. McPhaden, 2006: Wind stress variations and interannual sea surface temperature anomalies in the eastern equatorial Pacific. *J. Climate,* **19,** 226–241.